Shapley Additive Explanations for Knowledge Discovery in Aerodynamic Shape Optimization

Satoshi Takanashi[*], Shinsuke Nishimura[†], Kaoruko Eto[‡],
and Keita Hatanaka[§]

Mitsubishi Heavy Industries, Ltd., Oye-cho, Nagoya, Aichi, 455-8515, Japan

Explainable artificial intelligence (xAI) is a recently growing subfield of machine learning (ML), which focuses on providing rationales for results of ML models. By applying methods known as feature importance-based xAI methods to ML models, it is possible to evaluate the contribution of each feature to the output. In this paper, Shapley additive explanations (SHAP), which is a feature importance-based xAI method derived from the coalitional game theory, is applied to Gaussian process models used in aerodynamic shape optimization (ASO) of transonic airfoils and commercial aircraft winglets. The results revealed that SHAP can be effective in extracting useful knowledge from ASO results, such as global and local sensitivity of design variables to the objective functions, presence of interaction between design variables, and tradeoff between objective functions.

I. Introduction

Aerodynamic shape optimization (ASO) is a method used to maximize the performance of an aerodynamic shape under certain design conditions. It is often conducted by combining computational fluid dynamics (CFD) with numerical optimization techniques. Popular optimization techniques in the field of ASO can be classified into two categories: gradient-based and gradient-free algorithms [1].

Gradient-based algorithms use gradients of objective and constraint functions with respect to design variables. This type of algorithms is especially advantageous for problems with a large numbers of design variables when gradient information is computed using efficient adjoint solvers [2, 3]. However, since gradient-based algorithms expect relatively smooth functions and precise gradient evaluation, they tend to require more effort to set up and run compared to gradient-free algorithms [1, 4]. Additionally, gradient-based algorithms focus on achieving the optimum solution rather than exploring the entire design space, which can make it difficult to extract global trends of the design space from data obtained by optimization.

Gradient-free algorithms only require values of the objective and constraint functions. In the field of ASO, gradient-free algorithms are commonly used in conjunction with surrogate models, such as Gaussian Processes (GPs), radial basis functions, and artificial neural networks. The idea of surrogate models is to replace expensive function evaluations (e.g., CFD) with computationally cheap models that approximate the output of these functions based on carefully selected sample points. Some surrogate models provide not only the prediction of the function values, but also the uncertainties of the prediction. These uncertainties can be exploited for efficient optimization using Bayesian optimization (BO) that has been found to perform well in a wide range of engineering fields [5, 6] and has thus gained popularity in the field of ASO [7, 8].

When conducting BO, the intermediate shapes obtained in the process of optimization are equally as important as the optimal shape. Useful design knowledge of the design space, such as the effect of design variables on the objective functions and the tradeoff between objective functions, can be extracted by analyzing the dataset of shapes. Designers can then use such knowledge to understand why certain shapes are efficient at improving performance, which will help in scenarios where designers need to decide which shape to choose from a pareto-optimal set of shapes or decide which design variables to add or remove in the next iteration of ASO. Therefore, while they are not as computationally

---

[*] Engineer, Fluid dynamics No.3 laboratory, satoshi.takanashi.t3@mhi.com
[†] Engineer, Fluid dynamics No.3 laboratory, shinsuke.nishimura.4c@mhi.com
[‡] Engineer, Fluid dynamics No.3 laboratory, kaoruko.eto.7k@mhi.com
[§] Manager, Fluid dynamics No.3 laboratory, keita.hatanaka.jv@mhi.com

efficient as gradient-based algorithms, there is still a strong demand for gradient-free algorithms with surrogate models (e.g., BO) from the perspective of knowledge discovery.

In past researches, knowledge discovery techniques, such as the scatter plot matrix (SPM) [7], the functional analysis of variance (ANOVA) [8, 9], and the self-organizing map (SOM) [9-11], have shown to be effective at extracting useful knowledge from optimization results [12, 13]. However, although these methods are useful for extracting certain aspects of the design space, they also have limitations. For instance, knowledge extraction with SPM becomes difficult as the number of variables increases. In such cases, the Pearson correlation coefficient can be used to help identify pairs of variables with strong relationships. However, this method only helps to identify linear relationships and does not perform well when the relationship is non-linear. Additionally, while ANOVA is helpful at obtaining the sensitivity of each design variable to the objective function in a quantitative manner, it does not provide information on whether the change in the design variable has a positive or negative effect on the objective function. Furthermore, while SOM works well at revealing tradeoff relationships between objective functions, the process can be subjective since tradeoff relationships are often identified by visually comparing color patterns on multiple charts.

Explainable artificial intelligence (xAI) [14, 15] is a rapidly growing subfield in machine learning (ML) and artificial intelligence (AI). Generally speaking, xAIs are methods that provide rationales for results of ML models and help humans interpret why certain predictions are made by the models. One of the main explanations made by xAI methods is feature importance. By applying feature importance-based xAI methods to black-box ML models, it is possible to evaluate contribution of each feature to the output. Since ASO with BO often use ML models (e.g., GP) as a surrogate model for CFD evaluation, these types of xAI methods can be applied to ASO results to estimate the impact of each design variable on the objective values.

In this paper, Shapley additive explanations (SHAP) [16], which is a feature importance-based xAI method derived from the coalitional game theory, is applied to ASO results. It will be shown how SHAP can be effective at extracting useful design knowledge from ASO results, such as the global and local sensitivity of design variables to the objective functions, presence of interaction between design variables, and tradeoff of objective functions.

The remaining of this paper is organized as follows: Section II describes the BO method used by the authors. Section III explains the theory of SHAP. Section IV shows results of xAI methods applied to the drag minimization of the RAE2822 in transonic viscous flow. Section V describes results of xAI methods applied to the multidisciplinary design exploration of a commercial aircraft winglet. Section VI discusses the conclusion of this research.

II. Bayesian Optimization

Bayesian optimization is a well-known method for sequential optimization of computationally expensive black box functions. The procedure of BO mainly consists of two parts. The first part is constructing a model of the black box function, known as surrogate models. The second part is extracting promising candidates based on acquisition functions, also called infilling.

The following parts of this section provide an overview of the BO code developed by the authors (MHI-BO code) [17]. It should be noted that this code is written in Python and takes advantage of open-source GP and BO libraries such as GPyTorch [18] and BoTorch [19].

A. Surrogate Model

The success or failure of BO greatly depends on the accuracy of the surrogate model. One of the most popular surrogate models is the GP (i.e., Kriging) which allows to evaluate statistical relationships between design variables and objective functions. In the MHI-BO code, three types of surrogate models are available for BO: ordinary Gaussian process (OGP), deep Gaussian process (DGP) [20], and deep sigma point process (DSPP) [21]. In Ref. [17], the performance of these surrogate models was compared in numerical benchmark functions and optimization of transonic airfoils. The results showed that the performance of DGP and DSPP were sensitive to hyperparameter settings (e.g., number of hidden layers), and in many cases, DGP and DSPP showed lower performance than OGP, which was thought to be caused by insufficient tuning of the hyperparameters. Methods such as grid search can be utilized to tune hyperparameters of DGP and DSPP for each optimization problem but would often be too time-consuming for practical use cases in engineering problems. Therefore, OGP, which has fewer hyperparameters to adjust than DGP and DSPP, is thought to be more robust for engineering applications; for this reason, OGP was applied in Section IV of this study.

With OGP, an unknown function f (e.g., objective function) is modeled as follows

$$f \sim GP(\mu, k) \tag{1}$$

where μ is the mean function and is constant for OGP, and k is the kernel function. In this paper, the Matérn 5/2 kernel, a kernel commonly used in the field of data science, was used. The Matérn 5/2 kernel is given as

$$k(x,x') = \theta_{out}\frac{2^{1-\nu}}{\Gamma(\nu)}\left(\sqrt{2\nu}r\right)^{\nu}K_{\nu}\left(\sqrt{2\nu}r\right) \tag{2}$$

where $\nu = 5/2$, $r = |x - x'|/\theta_{len}$, θ_{out} is output scale, θ_{len} is length scale, Γ is the gamma function, and K_{ν} is the modified Bessel function. The hyperparameters μ and θ are optimized by a gradient-based algorithm based on maximum likelihood estimation. When n sample points in d dimensions are provided, the predictive mean $\hat{y}$ and predictive standard deviation $\hat{s}$ of a new sample point x^* are expressed as follows

$$\hat{y}(x^*) = \mu + K(x^*,X)^T(K(X,X) + \sigma^2 I)^{-1}(y - \mu) \tag{3}$$

$$\hat{s}^2(x^*) = K(x^*,x^*) + K(x^*,X)^T(K(X,X) + \sigma^2 I)^{-1}K(x^*,X) \tag{4}$$

where X is a $n \times d$ matrix where the ith row is the design variables of the i-th sample x^i, y is a n-dimensional vector where the i-th element is $f(x^i)$, $K(X,X)$ is a $n \times n$ matrix where $[K(X,X)]_{ij} = k(x_i,x_j)$, $K(x^*,X)$ is a n-dimensional vector where $[K(x^*,X)]_i = k(x^*,x_i)$, and $\sigma^2 I$ is a $n \times n$ diagonal matrix representing the amount of noise included in the observations of f.

B. Acquisition Function

In BO, exploration and exploitation of the design space are balanced using acquisition functions. Built on BoTorch, the MHI-BO code takes advantage of state-of-the-art acquisition functions, such as q-expected improvement (qEI) [22], q-Expected Hypervolume Improvement (qEHVI) [23, 24], and qParEGO [23]. With these acquisition functions, it is possible to select multiple (q) candidates per Bayesian optimization loop, which helps to accelerate the actual execution time of the optimization process. The q candidates are selected using the greedy approach [25], where instead of finding q sets of design variables which maximize the acquisition function in one joint optimization, q sequential optimizations are performed. This approach is beneficial for cases with large q where the joint optimization becomes difficult to solve due to the increasing dimension of the problem. In each stage of the sequential optimization, multi-start gradient descent with exact gradients evaluated by automatic differentiation is used to find the optimal set of design variables with regard to the acquisition function.

The direct and indirect methods are available for constraint handling. In the former method, the constraint is directly evaluated, and the gradient descent algorithm respects this constraint. This method is useful for cases where constraints can be easily evaluated from design variables (e.g., constraint on the thickness of an airfoil). In the latter method, constraints are modeled by a surrogate model, and the acquisition function is suppressed to zero when the surrogate model predicts that constraints are violated. This method is useful for cases where evaluation of constraints is computationally expensive (e.g., constraint on the pitching moment coefficient of an airfoil).

III. Shapley Additive Explanations

Shapley additive explanations is a model-agnostic approach which aims to provide an explanation of a prediction (e.g., objective functions) by estimating contribution of each feature (e.g., design variables) to the prediction. Our idea is to understand the relationship between objective functions and design variables by applying SHAP to surrogate models created in BO.

In SHAP, the original model $f(x)$ (e.g., GP) is approximated by a local linear model $g(x')$ given as

$$g(x') = \phi_0 + \sum_{j=1}^{M} \phi_j x'_j \tag{5}$$

where $x' \in \{0,1\}^M$ is the simplified binary features that is mapped to the original features x with a mapping function $x = h(x')$, M is the number of features, ϕ_0 is the mean model prediction (i.e., the mean value of $f(x)$ for the entire dataset), and ϕ_j is a coefficient denoting the contribution of the j-th feature to the prediction. In Ref. [16], three desirable properties for this local linear model are explained: local accuracy, missingness, and consistency. Local accuracy means that the local linear model matches the original model when x' is all set to one.

$$f(x) = g(1) = \phi_0 + \sum_{j=1}^{M} \phi_j \tag{6}$$

Missingness means that the coefficient of a missing feature is zero.

$$x_j' = 0 \Rightarrow \phi_j = 0 \tag{7}$$

Consistency means that if a model is changed so that the contribution of a feature increases or stays the same, the corresponding coefficient also increases or stays the same. This can be expressed as

$$f_x'(x') - f_x'(x'\backslash j) \geq f_x(x') - f_x(x'\backslash j) \Rightarrow \phi_j(f', x) \geq \phi_j(f, x) \tag{8}$$

where f and f' are arbitrary models, $f_x(x') = f(h(x'))$, and $x'\backslash j$ indicates setting $x_j' = 0$.

The only solution that satisfies these properties is Shapley values [26], which is a method from the coalitional game theory used to assign payouts to players depending on their contribution to the total payout. Shapley values are calculated with the following equation

$$\phi_j(f, x) = \sum_{z' \subset x'} \frac{|z'|! \, (M - |z'| - 1)!}{M!} [f_x(z') - f_x(z'\backslash j)] \tag{9}$$

where $|z'|$ is the number of non-zero elements in z', and $z' \subset x'$ denotes to all possible combinations of z' where the non-zero elements are a subset of the non-zero elements in x'. A simplified explanation of this equation would be that the contribution of the j-th feature is calculated by averaging the difference in the model prediction with or without knowledge of the j-th feature for all possible subsets of the simplified binary features. Here "with knowledge" (i.e., $z_j' = 1$) means that the value of the corresponding feature (x_j) is used when calculating the function value ($f(x)$), whereas "without knowledge" (i.e., $z_j' = 0$) means that the effect of the corresponding feature is marginalized. This is somewhat analogous to partial dependence plots [27] that visualize the main effect of features by marginalizing the effect of all other features.

Note that in this research, Shapely values were calculated using the open-source Python library SHAP [16]. Also, an example of SHAP applied to a simple linear analytic function is provided in Appendix A to help readers understand the process of knowledge extraction with SHAP.

IV. Application to the Drag Minimization of the RAE2822 in Transonic Viscous Flow

A. Problem Definition
In order to demonstrate the capability of SHAP applied to ASO, drag minimization of the RAE2822 in transonic viscous flow, which is one of the benchmark aerodynamic optimization problems provided by the AIAA aerodynamic design optimization discussion group (ADODG) [28], was selected as a test problem to analyze. In this optimization problem, the drag coefficient (C_d) of the RAE2822 airfoil is minimized at a freestream Mach number of 0.734, Reynolds number 6.5×10^6, lift coefficient (C_l) 0.824 with constraints on the pitching moment coefficient at the quarter-chord (C_m) and cross-sectional area ($Area$). The problem is summarized as follows:

$$
\begin{aligned}
\min \; & C_d \\
s.t. \; & C_l = 0.824 \\
& C_m \geq -0.092 \\
& Area \geq Area_{RAE2822}
\end{aligned} \tag{10}
$$

B. Computational Method
The Stanford University Unstructured (SU2) suite [3] was used to solve the Reynolds-averaged Navier-Stokes (RANS) equations. Discretization of the governing equations was done with the finite volume method with an edge-based data structure. The convective terms were evaluated by the Roe scheme [29] with 2nd order MUSCL. The turbulent viscosity was modeled by the Spalart-Allmaras model [30]. The spatial gradients were evaluated by the Green-Gauss method. Time integration was done with the Euler implicit method.

An example of the unstructured mesh used in this study is shown in Fig. 1. The mesh consists of a prism layer around the airfoil and an unstructured triangular mesh for the remaining area. The off-wall spacing was 4×10^{-6} in order to achieve y+ < 1. The far-field was 50 chords away. The result of the mesh convergence study is summarized in

Table 1. It was confirmed that C_d decreases monotonically as the number of nodes increased. The L2 mesh was selected as a good compromise between accuracy and computational cost.

Table 1 Summary of the mesh convergence study

Mesh	# of total nodes	# of nodes on the airfoil surface	C_l	C_d [cts]
L0	7391	164	8.240	265.1
L1	15983	244	8.240	229.0
L2	35946	365	8.240	205.3
L3	80721	547	8.240	201.3

a) **Entire flowfield**   b) **Close to airfoil**
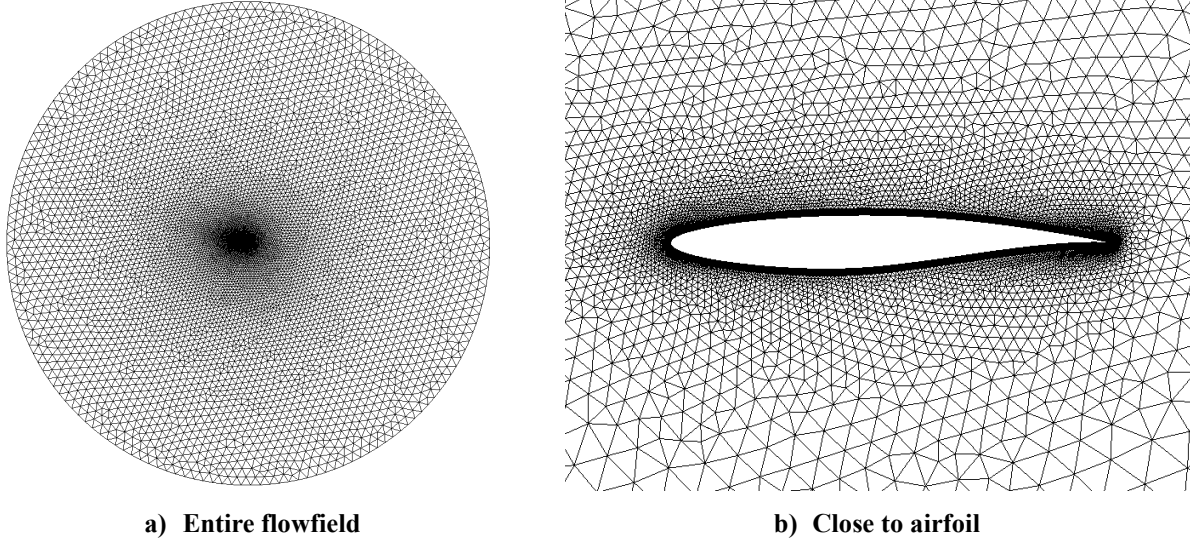
Fig. 1 Computational mesh (L2 mesh).

C. Geometry Parametrization

The geometry of the airfoil was represented using the Class Shape Transformation (CST) method [31]. In the CST method, a round-nose and pointed-aft-end airfoil is defined by the class function $C_{1.0}^{0.5}(\psi)$ and shape function $S(\psi)$ using the following equations

$$\zeta(\psi) = C_{1.0}^{0.5}(\psi) \cdot S(\psi) + \psi \cdot \Delta\zeta_T \tag{11}$$

$$C_{1.0}^{0.5}(\psi) = \sqrt{\psi}(1 - \psi) \tag{12}$$

$$S(\psi) = \sum_{i=0}^{n}(A_i \cdot K_i \cdot \psi^i (1-\psi)^{n-i}) \tag{13}$$

where ψ and ζ are the x and z-coordinates, $\Delta\zeta_T$ is trailing edge thickness, n is the order of the Bernstein polynomial, A_i is the weight of each term in the shape function, and K_i is the Binominal coefficient.

For this study, in order to make knowledge extraction results human friendly, instead of directly manipulating the weights A_i of the shape function, intuitive parameters based on the PARSEC method [32] were used to define the airfoil which were afterwards mapped to the weights A_i with a method based on Ref. [33]. In this method, the airfoil is first defined using the nine parameters shown in Table 2 and Fig. 2. Assuming $n = 4$ and $\Delta\zeta_T = 0$ for Eq. (11), functions that represent the upper and lower surface of the airfoil (ζ_u and ζ_l) are shown as follows

$$\zeta_u(\psi) = \sum_{i=0}^{4}(A_{ui} \cdot K_i \cdot \psi^{i+0.5}(1-\psi)^{n-i+1}) \tag{14}$$

$$\zeta_l(\psi) = \sum_{i=0}^{4} \left(A_{li} \cdot K_i \cdot \psi^{i+0.5}(1-\psi)^{n-i+1} \right) \tag{15}$$

Then the weights of the shape functions A_{ui} and A_{li} can be calculated by solving the following equations.

$$A_{u0} = -A_{l0} = \sqrt{2r_{le}} \tag{16}$$

$$\zeta_{u,l}(x_{u,l}) = z_{u,l} \tag{17}$$

$$\left[\frac{d\zeta_{u,l}}{d\psi} \right]_{\psi=x_{u,l}} = 0 \tag{18}$$

$$\left[\frac{d^2\zeta_{u,l}}{d\psi^2} \right]_{\psi=x_{u,l}} = z_{xxu,xxl} \tag{19}$$

$$\left[\frac{d\zeta_u}{d\psi} \right]_{\psi=1} + \left[\frac{d\zeta_l}{d\psi} \right]_{\psi=1} = 2\tan\alpha_{te} \tag{20}$$

$$\left[\frac{d\zeta_u}{d\psi} \right]_{\psi=1} - \left[\frac{d\zeta_l}{d\psi} \right]_{\psi=1} = \tan\beta_{te} \tag{21}$$

The baseline values of the parameters were defined by least squares fitting of the RAE2822 airfoil. The upper and lower bounds of the parameters were defined as 80% to 120% of these baseline values as shown in Table 3.

Table 2 Parameters defining the airfoil

Parameter	Definition
r_{le}	Leading edge radius
x_u, x_l	Upper and lower crest location
z_u, z_l	Upper and lower crest value
z_{xxu}, z_{xxl}	Upper and lower curvature at crest location
α_{te}	Trailing edge angle
β_{te}	Trailing edge wedge angle

Table 3 Upper and lower bounds of the parameters

Parameter	Baseline value (Fit to RAE2822)	Lower bound	Upper bound
r_{le}[1]	0.008625	0.005308	0.011943
x_u	0.4314	0.3452	0.5177
z_u	0.06296	0.05037	0.07555
z_{xxu}[1]	-0.4491	-0.6218	-0.2763
x_l	0.3430	0.2744	0.4116
z_l	-0.05888	-0.07065	-0.04710
z_{xxl}[1]	0.7003	0.5602	0.8404
α_{te} [deg]	6.829	5.463	8.195
β_{te} [deg]	9.520	5.859	13.182

[1]: Since the change in curvature and radius have a squared root effect on the coordinates of the airfoil, the bounds of these variables were defined as 64% to 144% which are squared values of 80% and 120%.
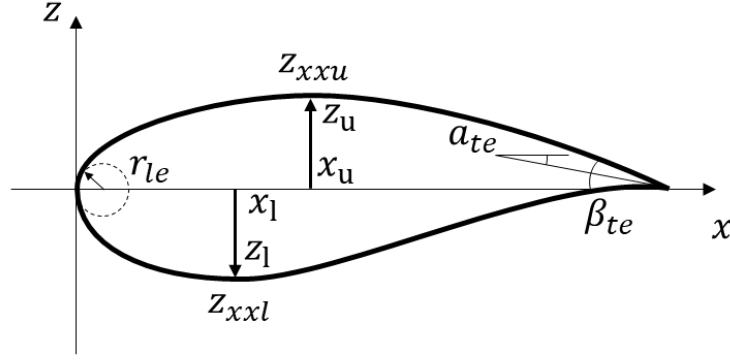
Fig. 2 Parameters defining the airfoil.

D. Optimization Method

Surrogate based optimization was performed using the MHI-BO tool. Ordinary Gaussian process with the Matérn 5/2 kernel was used to create surrogate models for C_d and C_m. The cross-sectional area of the airfoil was calculated by analytical integration of Eq. (14) and (15). The initial sample size was 90, which is 10 times the number of design variables. Initial samples were generated by optimal Latin hypercube sampling (LHS) [34] and are shown in Fig. 3. Additional samples were selected using the q-EI acquisition function. Thirty Bayesian optimization loops were conducted, and four additional samples were added in each loop. Constraints were handled by the direct method for cross-sectional area and the indirect method for C_m. The optimization method is summarized in Table 4.

Table 4 Summary of the optimization method

| Factor	Method/value
Surrogate model	Ordinary gaussian process with Matérn 5/2 kernel
Initial sample generation	Optimal Latin hypercube
Acquisition function	q-EI
Constraint handling	C_m: direct method, $Area$: indirect method
# of design variables	9
# of objectives	1
# of constraints	2
# of initial samples	90
# of Bayesian optimization loops	30
# of additional samples per loop	4
# of total samples	210
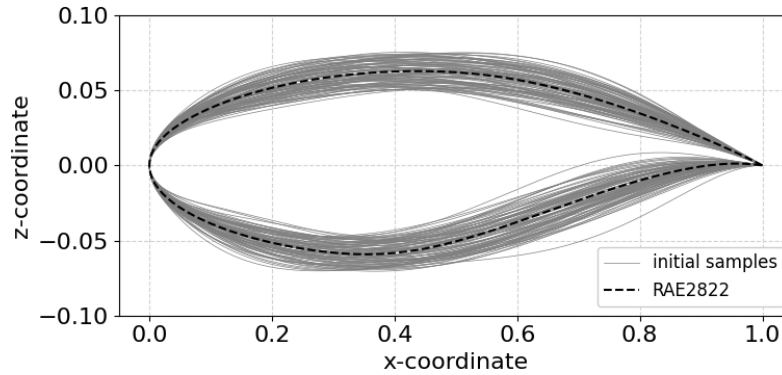
Fig. 3 Initial samples.

E. Optimization Result

The convergence history of C_d is shown in Fig. 4. The optimal airfoil was found on the 16-th loop and was able to achieve a 37.5% drag reduction as shown in Table 5. Comparisons of the airfoil geometry and pressure coefficient between the RAE2822 and the optimized airfoil are shown in Fig. 5. It can be seen that the strength of the shock wave on the upper surface of the airfoil is weakened with the optimized airfoil compared to that of the RAE2822.

Table 5 Optimization result of the RAE2822

Shape	C_l [-]	C_d [cts]	C_m [-]	$Area$ [-]	ΔC_d [cts]	ΔC_d [%]
RAE2822	0.8240	205.3	-0.0964	0.7787	-	-
Optimized	0.8240	128.4	-0.0901	0.7787	-76.9	-37.5
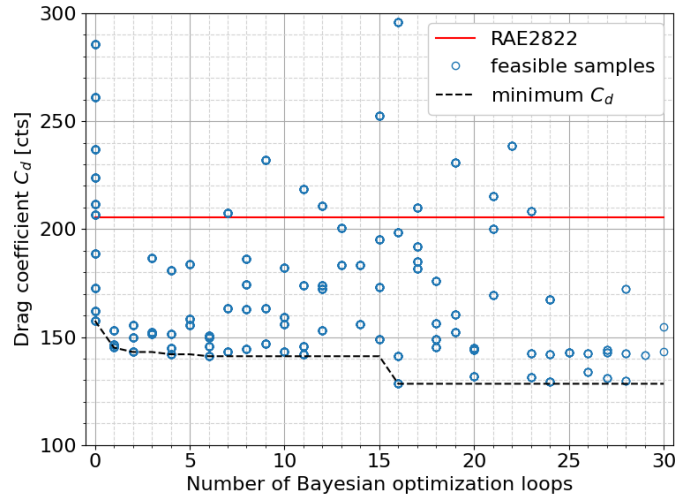
Fig. 4 Convergence history of C_d. The horizontal axis represents the number of Bayesian optimization loops, and the vertical axis represents the drag coefficient. The red solid line corresponds to the baseline value of RAE2822, the blue circles show samples that satisfied the constraints, and the black dashed line corresponds to the minimum C_d obtained at that point in the optimization. Note that the initial samples are shown as loop #0.
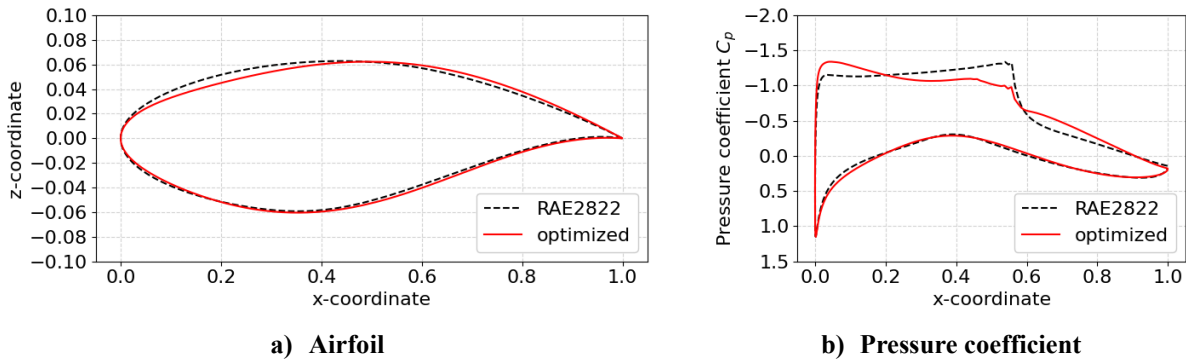

a) **Airfoil**

b) **Pressure coefficient**

Fig. 5 Comparison of the baseline RAE2822 and optimized airfoil.

F. Knowledge Discovery

First, design knowledge was extracted from the optimization result by conventional methods, namely SPM and ANOVA[*]. Figure 6 is an SPM of the nine design variables and the aerodynamic coefficients C_d and C_m. From this plot it can be observed that the upper crest location (x_u) has a fairly strong negative correlation to C_d, which indicates

---

[*] For readers unfamiliar with SPM and ANOVA, brief introduction to these methods are provided in Appendix B.

that an increase in upper crest location tends to reduce C_d. It can also be observed that upper crest value (z_u) has a strong negative correlation to C_m, which indicates that larger upper crest value results in pitch down C_m. Figure 7 shows results of ANOVA for C_d and C_m. For C_d, the upper crest location is the most dominant design variable followed by the lower crest value (z_l) and upper crest value. For C_m, the upper and lower crest values are the most dominant design variables.

Next, the global trend of the design space was analyzed using SHAP. Since sample points from the optimization tended to be concentrated near the optimal solution, 300 evenly distributed sample points were generated by LHS as substitutes. Then, SHAP values for C_d and C_m were then calculated using these new sample points, which helped remove the bias caused by unevenness of the original sample distribution. Figure 8 shows beeswarm plots of the SHAP values for C_d and C_m. By looking at the order of the design variables in the beeswarm plots, it can be seen that upper crest location, upper crest value, and lower crest value have the largest effect on C_d and C_m, which corresponds to what was found using ANOVA. Furthermore, by observing the SHAP value distributions, the contribution of each design variables to C_d and C_m can be assessed quantitatively. For example, the SHAP value distribution of upper crest location for C_d shows a linear trend where C_d decreases by 100 cts when the upper crest location is close to the upper bound and increases by 100 cts when the upper crest location is close to the lower bound, which agrees with findings from SPM. This trend occurs because when the upper crest location is shifted backwards, the curvature near the leading edge becomes larger, leading to a more pronounced negative pressure coefficient at the suction peak, which in turn acts as thrust that helps decrease C_d. Similar linear trends can be seen for $C_m - z_u$, which agrees with SPM, and also $C_d - z_u$ and $C_m - z_l$, which are relationships that were not apparent when using SPM.

As for the SHAP value distribution of the upper crest value for C_d, the trend is non-linear, and therefore a SHAP dependence plot (Fig. 9) is used to examine the details of this relationship. From this figure, it can be observed that the trend of upper crest value changes based on upper crest location. When the upper crest location is close to the lower bound (blue dots), SHAP value takes a minimum value when the upper crest value is around $z_u = 0.05$. On the other hand, when the upper crest location is close to the upper bound (red dots), SHAP value takes a minimum of around -50 cts at around $z_u = 0.06$ and increases to around 0 cts at $z_u = 0.05$. This indicates that, depending on the upper crest location, minimizing the upper crest value (i.e., minimizing the thickness of the upper half of the airfoil) does not always contribute to minimizing C_d. For airfoils with the upper crest location shifted downstream, C_d is minimized when the upper crest value close to the baseline value, which is beneficial for maintaining a sufficient cross-sectional area.

Finally, the local trend of the design space is analyzed using a SHAP. Figure 10 shows SHAP waterfall plots of C_d and C_m for the optimized airfoil. By looking into Fig. 10a, it is possible to comprehend why the optimized airfoil succeeded in achieving the minimum C_d. For the optimized airfoil ($C_d = 128.4$ cts), C_d is lower than the average airfoil ($C_d = 291.8$ cts) by 163.4 cts. Around 97 cts of this is caused only by upper crest location, followed by upper crest value, which contributes to around 40 cts in drag reduction. Lower crest value did not contribute much to drag reduction, although it showed a large sensitivity in Fig. 8. This is thought to be because the lower crest value is kept close to the baseline value in order to meet the constraint on cross-sectional area. While C_d is affected mostly by only upper crest location and value, various design variables contribute to the increase and decrease of C_m. For instance, lower crest location (x_l) only contributes to 2.8 cts in drag reduction, whereas it contributes to 0.004 decrease in C_m. This information can be beneficial for cases where small modifications need to be made on the optimized airfoil. For example, suppose that after the optimization process, the pitching moment constraint needed to be changed to a stricter value (e.g., $C_m \geq -0.088$). In such cases, designers can change the lower crest location to increase C_m, which would most likely result in a minimal increase in C_d.
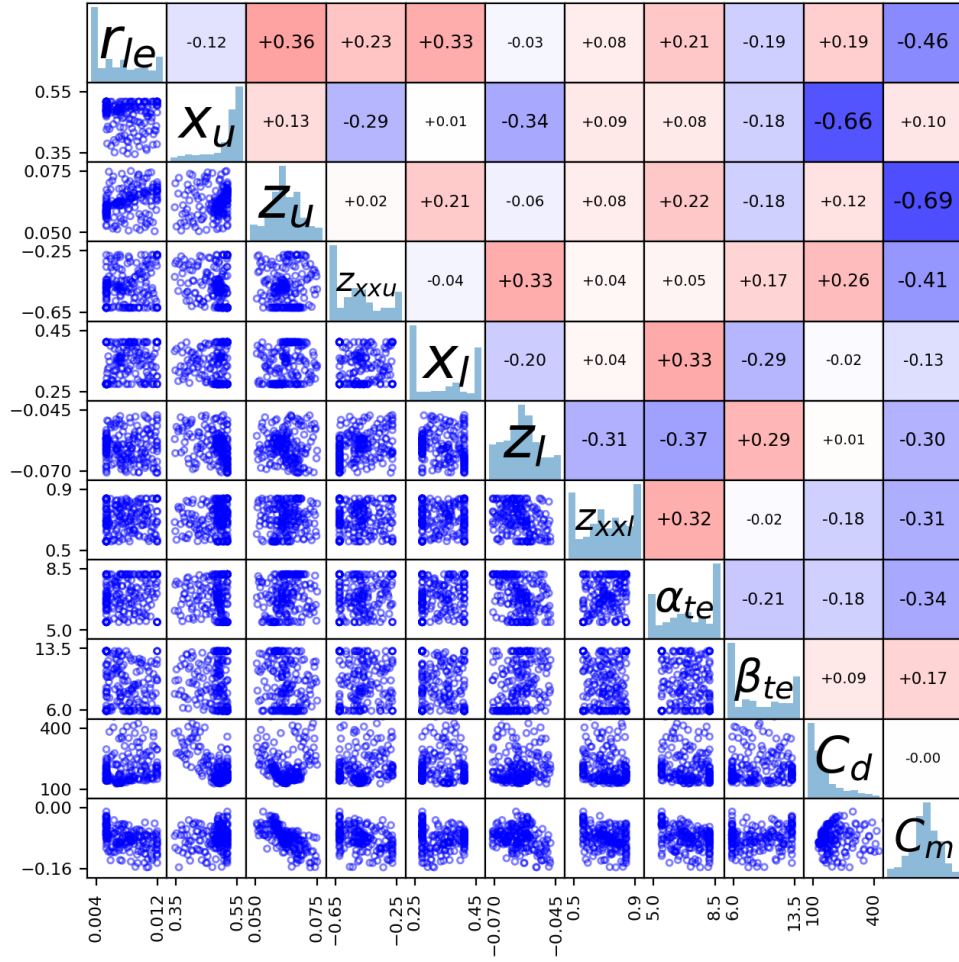
Fig. 6 SPM of the RAE2822 optimization result. The diagonal elements show histograms of the corresponding design variable or aerodynamic coefficient. The lower triangle shows scatter plots for each pair of design variables and aerodynamic coefficients and the upper triangle shows the Pearson correlation coefficient of these pairs.
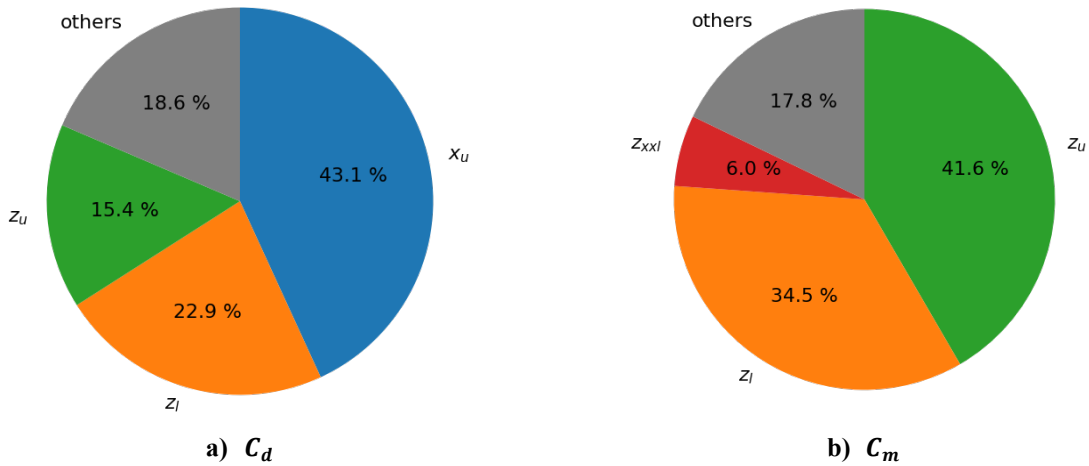

a) C_d

b) C_m

Fig. 7 ANOVA of the RAE2822 optimization result. Each slice shows the first-order sensitivity index of the corresponding design variable. First and second-order sensitivity indices lower than 5% are categorized into "others".

a) C_d

b) C_m
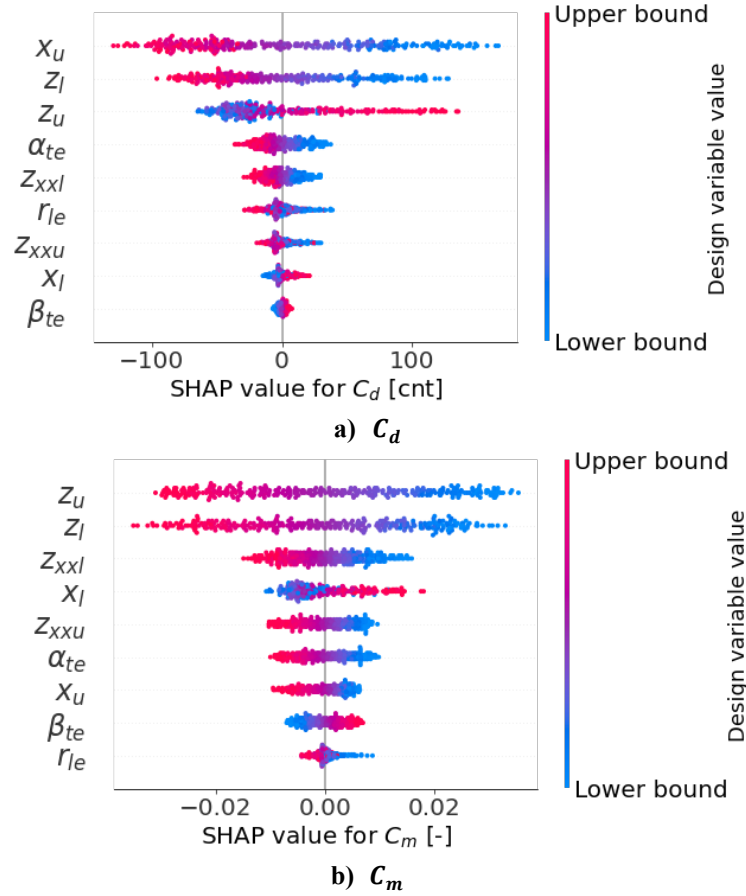
Fig. 8 SHAP beeswarm plot of the RAE2822 optimization result. Each row represents a single design variable. The design variables are sorted by their mean absolute SHAP value, meaning that C_d and C_m are more sensitive to the design variables at the top. Each dot corresponds to a sample point, and colors show whether the design variable of the sample point is closer to the upper bound (red) or closer to the lower bound (blue). The horizontal position of the dots indicates the SHAP value of each design variable for C_d and C_m. When many samples with the same SHAP value exist, the dots are stacked in vertical direction to show the density of the SHAP value distribution.
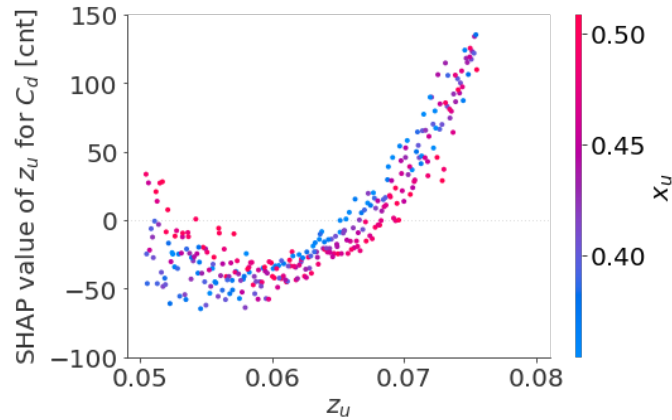
Fig. 9 SHAP dependence plot of upper crest value for C_d. The horizontal axis represents the upper crest value (z_u), and the vertical axis represents the SHAP value of upper crest value for C_d. The dots correspond to the sample points and are colored based on the value of upper crest location (x_u), which is the design variable with the largest interaction effect against upper crest value.
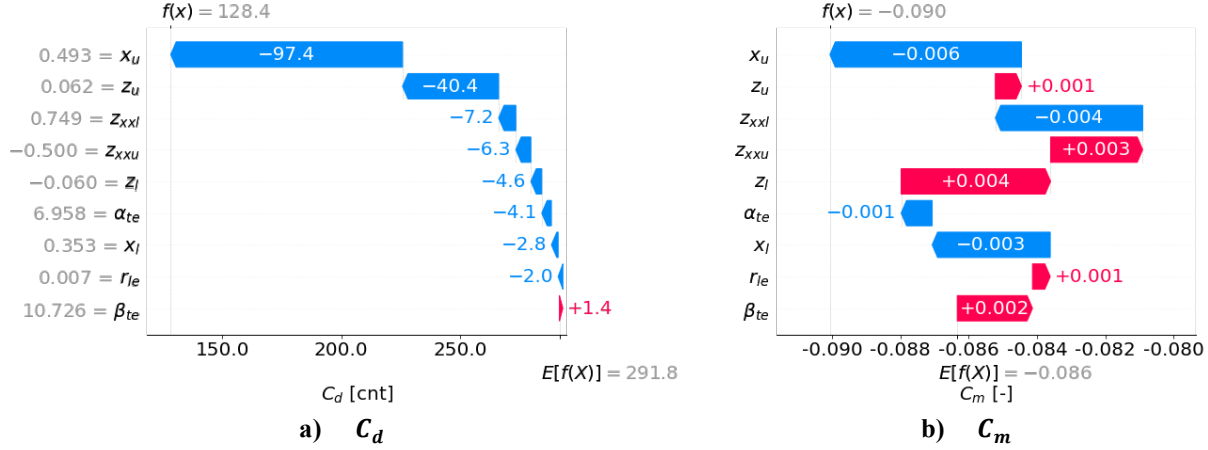
11

a) C_d
b) C_m

Fig. 10 SHAP waterfall plot of the optimized airfoil. The horizontal axis denotes the value of the objective function. Each row shows SHAP value of the optimized airfoil and how the positive (red) or negative (blue) contribution of each design variable moves the objective function value from the average of all samples ($E[f(x)]$) to the objective function value of the optimized airfoil ($f(x)$). The gray text on the left side of the design variable names shows the design variables of the optimized airfoil. In this figure, the design variables are sorted by their mean absolute SHAP value for C_d.

V. Application to the Multidisciplinary Design Exploration of a Commercial Aircraft Winglet

A. Problem Definition

In Ref. [35], a multidisciplinary design exploration of a commercial aircraft winglet was conducted, and the sensitivity of design variables was revealed using ANOVA. In this section, SHAP was applied to the same problem to investigate whether additional knowledge could be discovered with this new method.

In this problem, the winglet shape was defined by six design variables as shown in Fig. 11. Two functions, block fuel (ΔBF), which is the minimum fuel mass for a fixed range, and maximum takeoff weight ($\Delta MTOW$), which is related to the airport landing fee charged in some airports for commercial jets, were considered as objective functions to minimize. Note that ΔBF and $\Delta MTOW$ denote the difference from reference values shown as percentages. These objective functions were evaluated by an in-house performance analysis tool. In this tool, the aerodynamic drag and the wing box weight were inputs. The former was evaluated by an unstructured Euler CFD analysis and the midfield drag decomposition technique. The latter was a function of the structural weight penalty of the wing box due to winglet installation, which was estimated by MSC Nastran[*]. A total of 32 sample individuals were selected by LHS as shown in Fig. 12. For further details, the reader shall refer to Ref. [35].
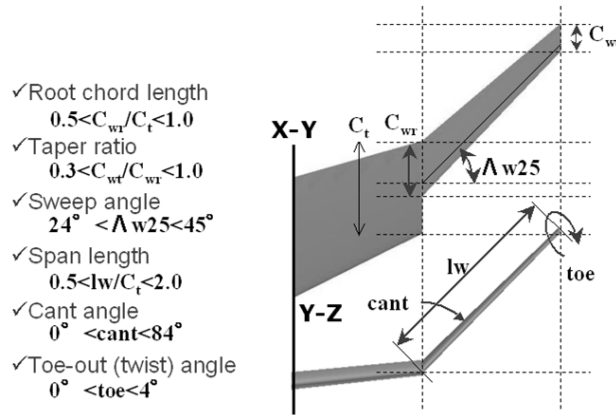

Fig. 11 Winglet shape definition (adapted from Ref. [35]).

---

[*] Detailed information of this software is available online at https://hexagon.com/products/product-groups/computer-aided-engineering-software/msc-nastran [retrieved 11 Nov 2022].
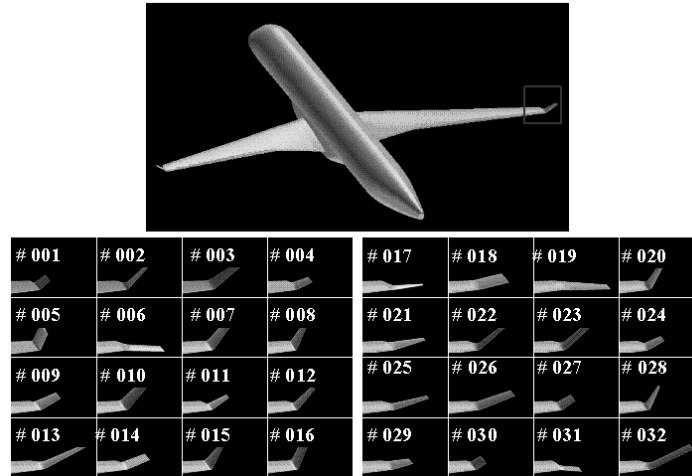
Fig. 12 Winglet shape of sample individuals (backward view, adapted from Ref. [35]).

B. Knowledge Discovery

First, knowledge discovery was conducted with SPM and ANOVA, shown in Fig. 13 and Fig. 14, respectively. The Pearson correlation coefficients in Fig. 13 show that the span length (lw/Ct) has a strong correlation between block fuel, where increase in span length is likely to decrease block fuel. This agrees with results of ANOVA in Fig. 14, which indicate that span length is the key design parameter for both objective functions and results in around 40% of the total variance of the design space. In addition to this, it can be observed that cant angle (*cant*), toe-out angle (*toe*), and sweep angle (Λ_{w25}) are the next most important parameters. These findings are reasonable from the aerodynamic perspective according to Ref. [35].

Next, knowledge discovery was conducted with SHAP. Since the original number of sample points was relatively small, 300 evenly distributed sample points were generated by LHS as substitutes, and SHAP values were calculated using these new sample points. Beeswarm plots of SHAP values are shown in Fig. 15. From this figure, it can be seen that span length has the most significant impact on both objective functions, followed by cant angle, toe-out angle, and sweep angle, which is consistent with results from SPM and ANOVA. Furthermore, Fig. 15 provides insight into the amount of contribution span length has on each objective function. For instance, if span length is close to the upper bound, block fuel can be reduced by around 1% compared to the average sample, and on the other hand, MTOW will increase by around 1%. In other words, span length is the main factor controlling the tradeoff between block fuel and MTOW. Further knowledge of other design variables can be easily obtained from Fig. 15 in the same manner. Now, the question naturally arises which design variables should be changed to minimize block fuel while minimizing the penalty for MTOW under the existence of a tradeoff relationship between these two objective functions. One possible solution is sweep angle. Figure 16 shows SHAP values of major design variables for block fuel and MTOW in the form of a scatter plot. It can be said that these plots visualize the tradeoff relationship caused by each design variable. While span length and cant angle show tradeoff between the two objective functions, setting the sweep angle at around 40 to 45 degrees has the potential to reduce block fuel and MTOW by up to 0.5 %. Toe angle can also be used to improve block fuel and MTOW simultaneously, where a 0.2% reduction in both objectives can be achieved with a toe angle around three degrees. The discussion in this section demonstrates that SHAP can be helpful in getting deeper knowledge for multi-objective optimization problems.

In addition to the global interpretations discussed above, SHAP was used to explore the local trends of the design space. In Ref. [35], one design candidate was selected as a result of the design exploration (hereafter referred to as the "designed" winglet). In Fig. 17, waterfall plots for the designed winglet are shown. From the figure, the designed winglet (ΔBF = -4.78%) achieves a block fuel which is lower than the average winglet (ΔBF = -3.58%) by 1.2%. This reduction of block fuel mainly comes from span length, cant angle, sweep angle, and toe angle, where the contribution of these parameters is -0.48%, -0.32%, -0.24%, and -0.18%, respectively. However, at the same time, a tradeoff between block fuel and MTOW occurs for span length and cant angle, where MTOW increases due to these parameters by 0.30% and 0.24 %, respectively. As for sweep angle and toe angle, desirable values are selected, where block fuel and MTOW can be reduced simultaneously. Thus, the designed winglet succeeds in improving block fuel while maintaining MTOW the same as the average winglet.

Finally, advantages of SHAP compared with conventional approaches, SPM and ANOVA, will be discussed. While SPM was useful for observing relationships between all design variables and objective functions in one chart, it was difficult to obtain useful design knowledge since most scatter plots did not show a clear trend. The Pearson correlation coefficient was used to help identify relationships, but this method was only useful for when there was a strong linear relationship. In addition to this, although ANOVA was effective at evaluating the global importance of each design variable to the objective functions in a quantitative manner, it did not provide information on whether a change in the design variable would result in a positive or negative effect on the objective function. On the other hand, SHAP was capable of not only identifying design knowledge that was revealed by SPM and ANOVA, but also knowledge that was not revealed by these conventional methods, such as the quantitative effect of design variables on the objective functions (e.g., span length is capable of reducing block fuel up to 1%), and tradeoff relationships between the two objective functions (e.g., span length is the main cause of tradeoff between block fuel and MTOW). In addition to this, SHAP was able to identify local trends of the design space, which was useful for explaining why the designed winglet was able to achieve an above-average block fuel reduction while minimizing the increase in MTOW.
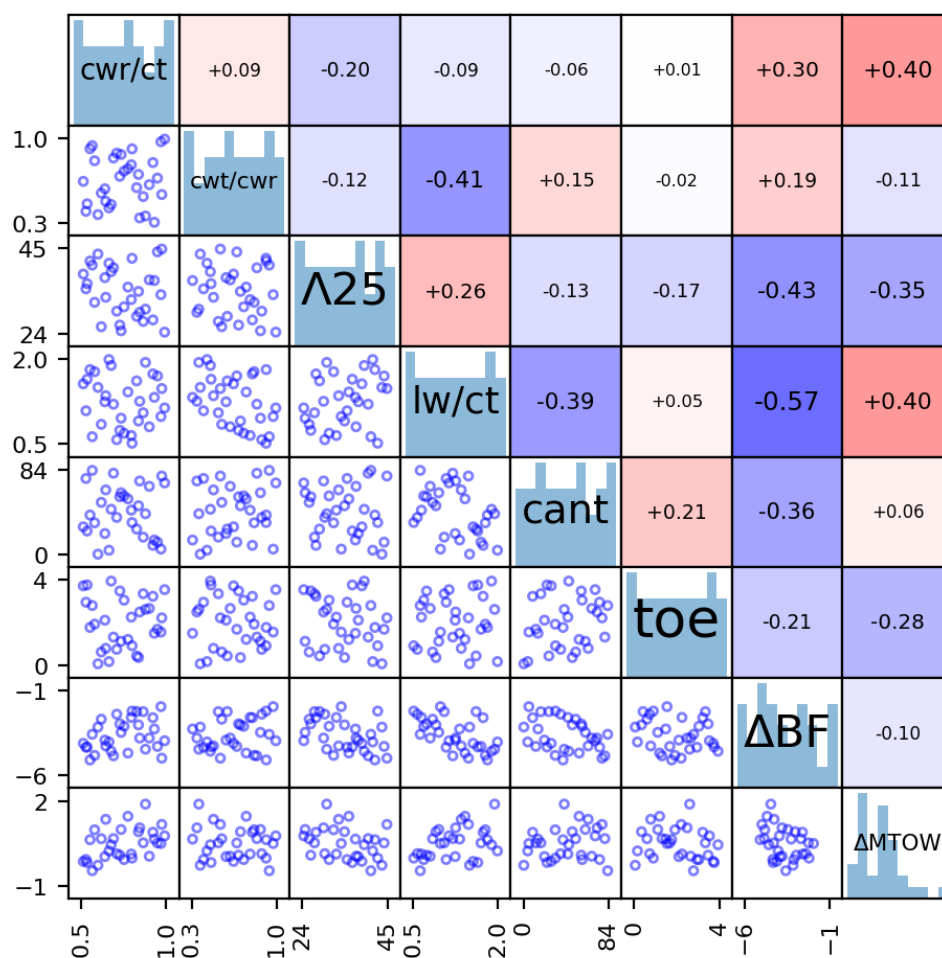

Fig. 13 SPM of the commercial aircraft winglet. The diagonal elements show the histogram of the corresponding design variable or objective function. The lower triangle shows scatter plots for each pair of design variables and objective functions and the upper triangle shows the Pearson correlation coefficient of these pairs.

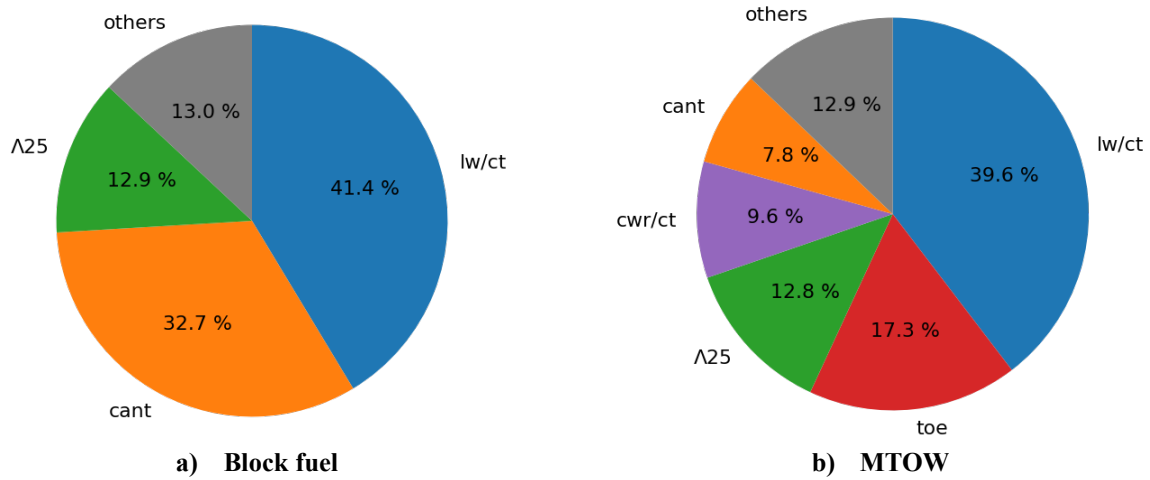a)   Block fuel   b)   MTOW

Fig. 14 ANOVA of the commercial aircraft winglet. Each slice shows the first-order sensitivity index of the corresponding design variable. First and second-order sensitivity indices lower than 5% are categorized into "others".
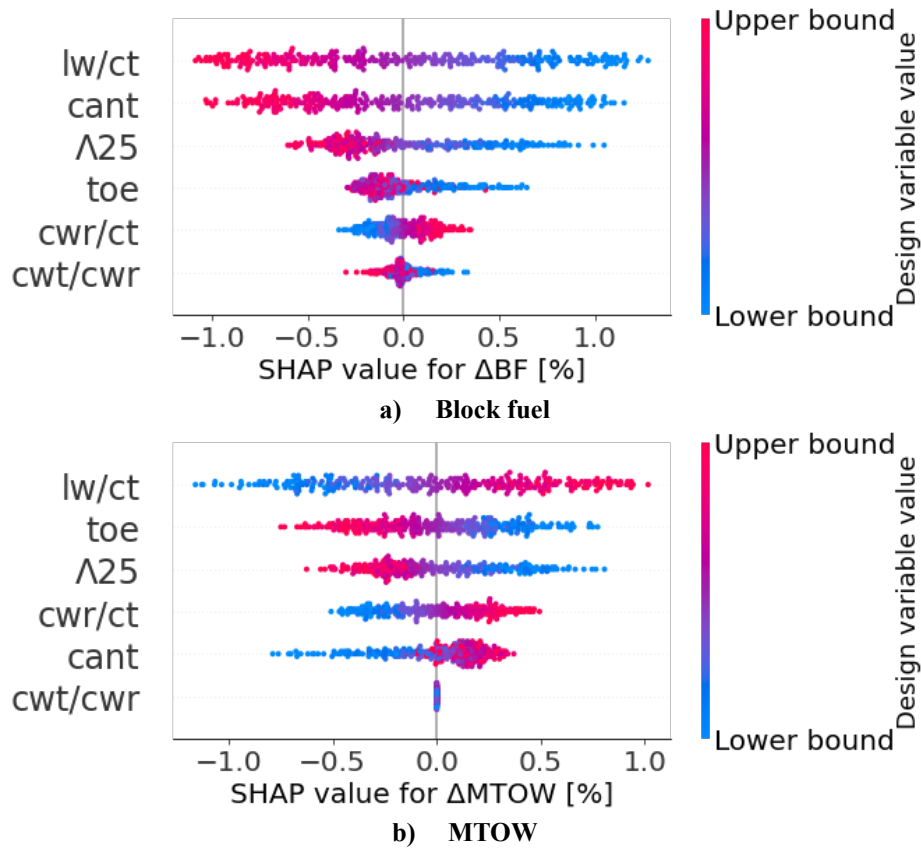

a)   Block fuel

b)   MTOW

Fig. 15 SHAP beeswarm plot of the commercial aircraft winglet. Each row represents a single design variable. The design variables are sorted by their mean absolute SHAP value, meaning that block fuel and MTOW are more sensitive to the design variables at the top. Each dot corresponds to a sample point, and colors show whether the design variable of the sample point is closer to the upper bound (red) or closer to the lower bound (blue). The horizontal position of the dots indicates the SHAP value of each design variable for block fuel and MTOW. When many samples with the same SHAP value exist, the dots are stacked in vertical direction to show density of the SHAP value distribution.
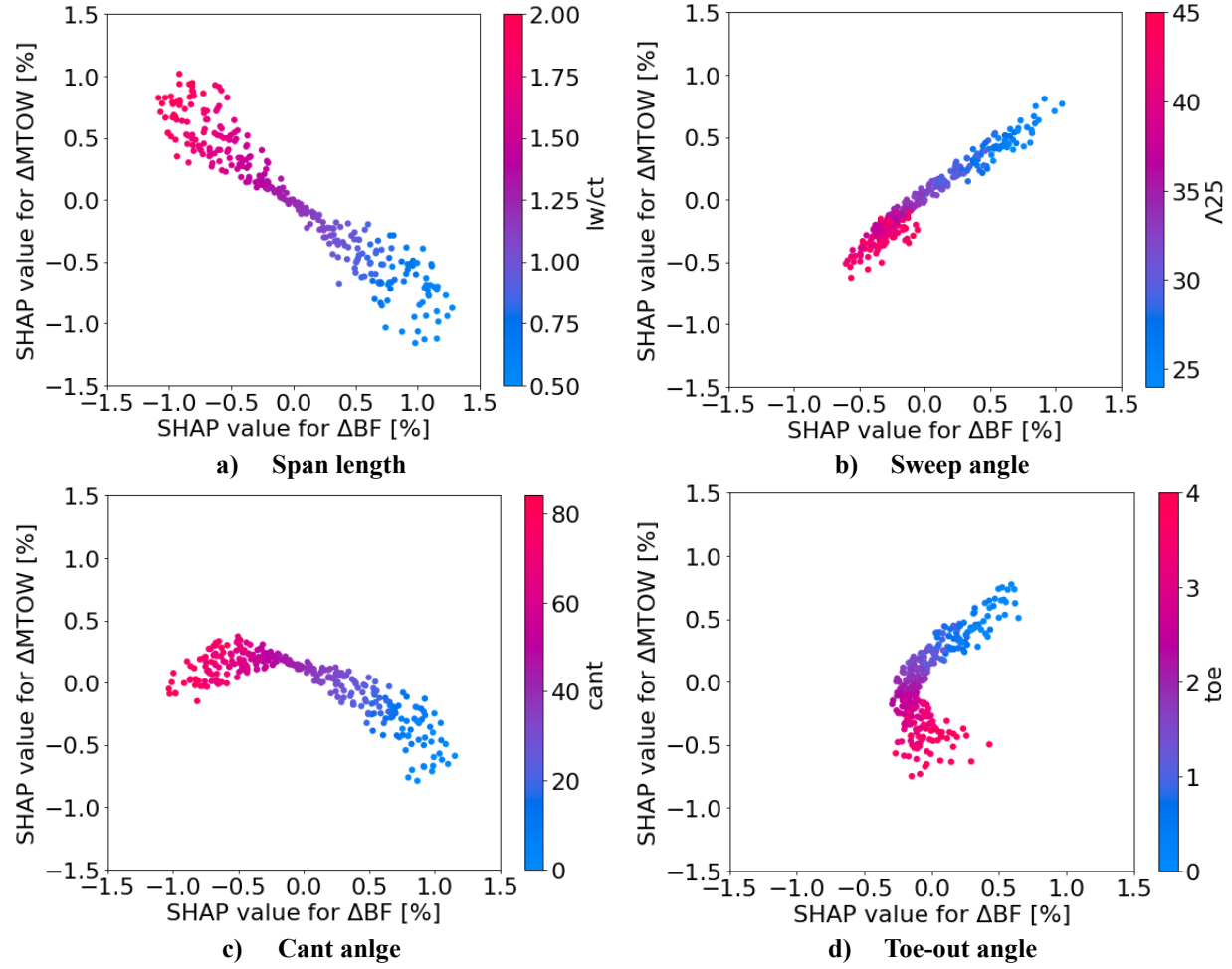
Fig. 16 SHAP tradeoff plot of the commercial aircraft winglet. The horizontal and vertical axis represent the SHAP value of block fuel and MTOW, respectively. The dots correspond to the sample points and are colored based on value of the design variable.
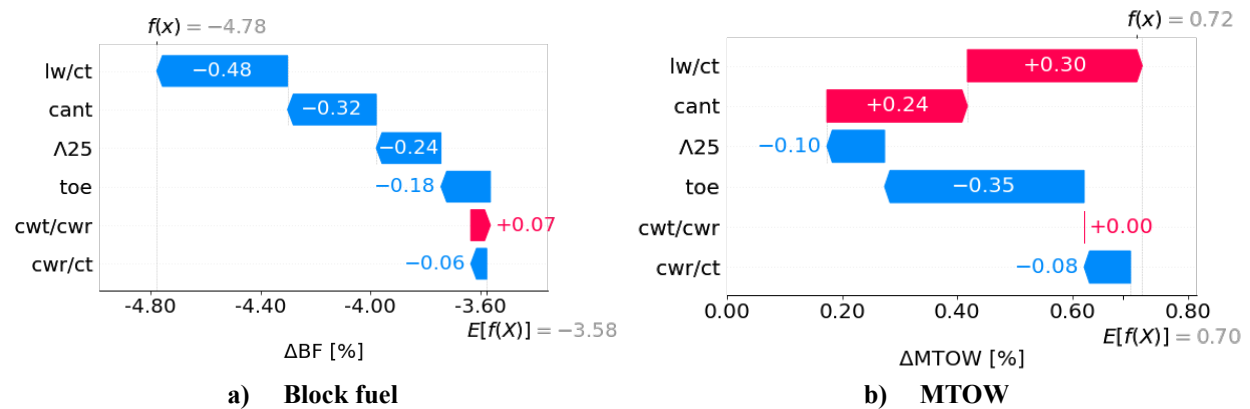

Fig. 17 SHAP waterfall plot of the designed winglet. The horizontal axis denotes the value of the objective function. Each row shows SHAP value of the designed winglet and how the positive (red) or negative (blue) contribution of each design variable moves the objective function value from the average of all samples ($E[f(x)]$) to the objective function value of the designed winglet ($f(x)$). In this figure, the design variables are sorted by their mean absolute SHAP value for block fuel.

16

VI. Conclusion

In order to investigate the effectiveness of SHAP for knowledge discovery in ASO, optimization results of a transonic airfoil and a commercial aircraft winglet were analyzed in this paper. In both cases, SHAP was successful in revealing knowledge that could be obtained from conventional data mining methods (i.e., SPM and ANOVA); for instance the presence of strong linear relationships between design variables and objective functions and the global sensitivity of design variables on the objective functions. In addition, SHAP was able to uncover furthermore details of the design space, such as the quantitative effect of the design variable on the objective function, locations of the design space where interaction between design variables is large, and the main cause of tradeoff between objective functions. With SHAP, it was also possible to analyze the local trends of the design space, which helped understand why particular sets of design variables resulted in an optimal solution. These results show how the unique features of SHAP are beneficial for knowledge extraction from ASO results. It should be noted that, in most cases, SHAP is used to analyze the trend of design variables against a single function. In this paper, the idea of SHAP is expanded to multi-objective problems, where the global trend for tradeoff between multiple functions is explored using scatter plots of SHAP values.

Consequently, it was shown that our approach is promising for knowledge extraction from ASO and can provide deeper knowledges to the designer in a simple way. Further research is still necessary to exploit the full potential of SHAP for knowledge discovery in ASO. For example, SHAP interaction values can be utilized to gain a richer understanding of interaction effects between design variables [36]. Also, supervised clustering based on SHAP values could be used to reveal distinctive groups that were not apparent with conventional clustering [36].

Appendix A: Shapley Additive Explanations Applied to a Linear Analytic Function

In this appendix, an example of SHAP applied to a linear analytic function is shown to help readers understand how design knowledge is extracted using SHAP. A linear analytic function $f(x)$ with five variables is given as

$$f(x) = 2 + \sum_{i=1}^{5} w_i x_i, \tag{A.1}$$

where $x_i \in [-1, 1]$, and w_i is the slope coefficient of each variable where $w = (-2, -1, 0, 1, 2)$. One hundred sample points were generated by LHS, and the output of the function was calculated at each sample point with Eq. (A.1). An ordinary gaussian model was trained based on these samples and analyzed using SHAP.

A beeswarm plot of SHAP values is shown in Fig. A.1. In this figure, the global trend of the design space is shown in a quantitative manner. First, the order of the design variables shows that the global sensitivity is largest for x_1 and x_5, followed by x_2 and x_4, and smallest for x_3, which corresponds to the absolute values of the slope coefficient of each variable. Next, the color and horizontal position of the dots show quantitative effects of each design variable where:

- x_1 has a negative correlation with the response and its quantitative impact is from -2 to 2.
- x_5 has a positive correlation with the response and its quantitative impact is the same as that of x_1.
- x_2 has a negative correlation with the response and its quantitative impact is from -1 to 1.
- x_4 has a positive correlation with the response and its quantitative impact is the same as that of x_2.
- x_3 has no impact on the response, which means that the response does not change even if x_3 is changed.

These findings are consistent with Eq. (A.1), which indicate that SHAP is capable of interpreting the global impact of each variable on the function.

A waterfall plot displaying SHAP values of the sample point with the largest function value is shown in Fig. A.2. In this figure, the local trend of the design space is shown in a quantitative manner. It can be observed that this sample point achieves a function value of 5.42, which is higher than the average function value (i.e., the intercept of Eq. (A.1), since it is a linear function). This increase in the function value is mainly caused by x_1, which contributes to increasing the function value by 1.98. This is consistent with the analytic value obtained from Eq. (A.1), where $w_1 \times x_1 = -2 \times (-0.99) = +1.98$. In addition, it can also be observed that the contribution of x_2 is larger than x_5, which is different from the global sensitivities shown in the beeswarm plot. This difference occurs, since x_2 is close to the lower bound, while the absolute value of x_5 is close to zero. These results indicate that SHAP is capable of interpreting the local sensitivities of each design variables around a certain sample point.
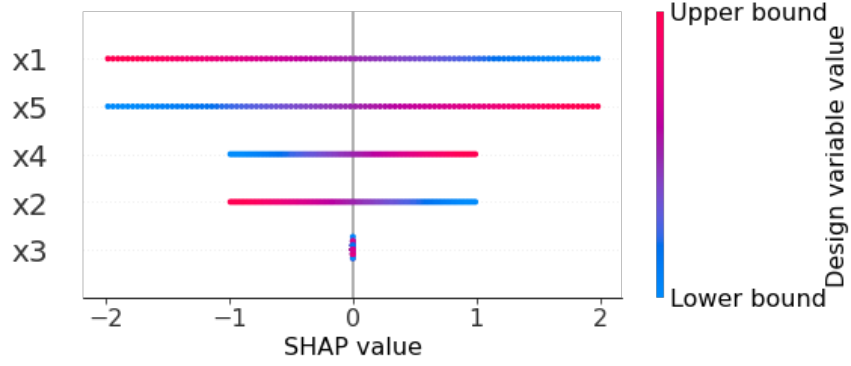
Fig. A.1 SHAP beeswarm plot of the linear analytic function. Each row represents a single design variable. The design variables are sorted by their mean absolute SHAP value, meaning that the function value is more sensitive to the design variables at the top. Each dot corresponds to a sample point, and colors show whether the design variable of the sample point is closer to the upper bound (red) or closer to the lower bound (blue). The horizontal position of the dots indicates the SHAP value of each design variable. When many samples with the same SHAP value exist, the dots are stacked in vertical direction to show the density of the SHAP value distribution.
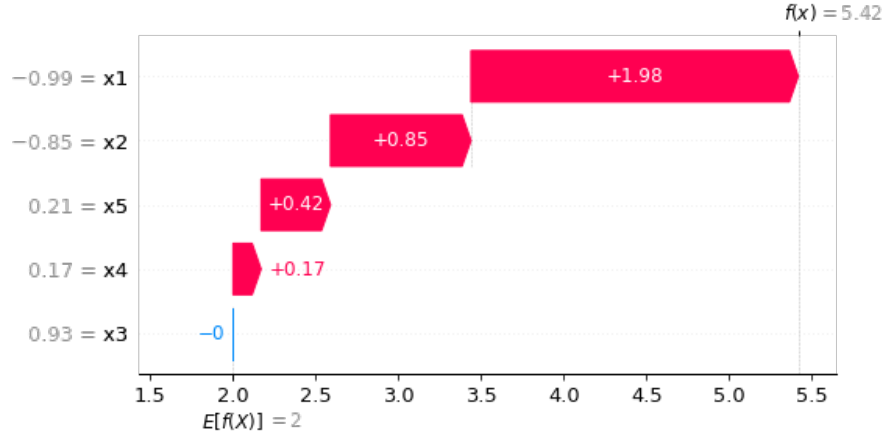

Fig. A.2 SHAP waterfall plot of the linear analytic function. The horizontal axis denotes the value of the objective function. Each row shows SHAP value of this sample and how the positive (red) or negative (blue) contribution of each design variable moves the objective function value from average of all samples ($E[f(x)]$) to the objective function value of the particular sample ($f(x)$). The gray text on the left side of the design variable names shows the value for this sample. In this figure, the design variables are sorted by their mean absolute SHAP value.

Appendix B: Conventional Knowledge Discovery methods for ASO

In this appendix, brief descriptions of the conventional data mining approaches utilized in this paper, scatter plot matrix (SPM) and functional analysis of variance (ANOVA), are provided.

B.1 Scatter plot matrix

In an SPM, scatter plots for each pair of variables are shown in the form of a matrix. In some cases, Pearson correlation coefficients and histograms are shown alongside these scatter plots to help understand the dataset. With an SPM, it is possible to assess the global relationship of many design variables and objective functions in one chart.

An example of SPM applied to the linear analytic function in Appendix A is shown in Fig. B.1. It can be seen that the variables x_1 and x_5 have fairly strong correlations with the function value (f). Considering that x_1 and x_5 have the largest slope coefficients in Eq. (A.1) ($w_1 = -2$ and $w_5 = 2$), it can be said that SPM succeeds to identify these strong linear relationships. It should be noted that while SPM is effective when the number of variables and function

18

values is small (a total of six for Fig. B.1), as the number increases it becomes difficult to identify relationships because the number of scatter plots begins to rapidly increase.
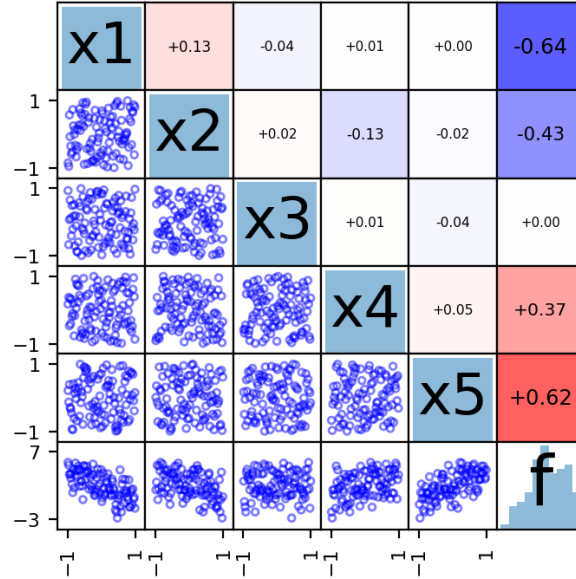

Fig. B.1 SPM of the linear analytic function in Appendix A. The diagonal elements show the histogram of the corresponding design variable or objective function. The lower triangle shows scatter plots for each pair of design variables and objective functions and the upper triangle shows the Pearson correlation coefficient of these pairs.

B.2 Functional Analysis of Variance

In ANOVA, the total variance of a model is decomposed into variance due to each design variable. By comparing the value of these variances, it is possible to identify which design variables have a large effect on the objective function in a quantitative manner. In this paper, decomposition is accomplished using Sobol′ indices [37, 38]. For a function $y = f(x)$ with an n-dimensional input $x = (x_1, x_2, ..., x_n)$, the first-order sensitivity index S_i, or in other words the main effect of the design variable x_i, can be written as

$$S_i = \frac{V[E(y|x_i)]}{V[y]} \qquad (B.1)$$

where $E(y|x_i)$ is the conditional expectation of y while keeping x_i fixed, and V denotes variance. In the same manner, the second-order sensitivity index S_{ij}, or in other words the interaction effect of the design variables x_i and x_j, can be expressed as

$$S_{ij} = \frac{V[E(y|x_i, x_j)]}{V[y]} - S_i - S_j \qquad (B.2)$$

where $E(y|x_i, x_j)$ is the conditional expectation of y while keeping x_i and x_j fixed. The indices S_i and S_{ij} are computed by the Monte Carlo approach. Note that the actual calculation in this paper was done using an open-source sensitivity analysis library, SALib [39, 40].

An example of ANOVA applied to the linear analytic function in Appendix A is shown in Fig. B.2. It can be seen that the relative amount of variance is 40% for variables x_1 and x_5, 20% for x_2 and x_4, and 0% for x_3. Considering that the variance of each variable increases in proportion to the squared value of the slope coefficients w_i in Eq. (A.1), it can be said that ANOVA succeeds to identify the sensitivity of the variables. However, it should be noted that ANOVA does not provide information on whether a change in the design variable has a positive or negative effect on

19

the objective function. For example, it is impossible to tell from the chart whether increase in x_1 will result in increase or decrease of the function value.
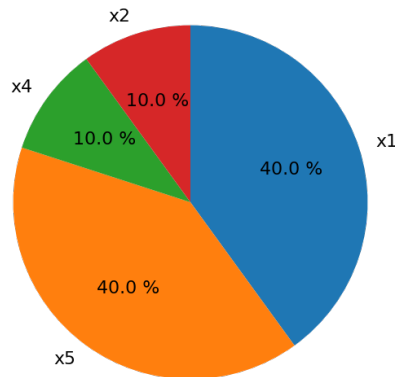

Fig. B.2 ANOVA of the linear analytic function in Appendix A. Each slice shows the first-order sensitivity index of the corresponding design variable.

Acknowledgements

References

[1]   Martins, J. R., and Ning, A., *Engineering design optimization*, Cambridge University Press, Cambridge, 2022.

[2]   Mader, C. A., Kenway, G. K., Yildirim, A., and Martins, J. R., "ADflow: An open-source computational fluid dynamics solver for aerodynamic and multidisciplinary optimization," *Journal of Aerospace Information Systems*, vol. 17, 2020, pp. 508–527.

[3]   Economon, T. D., Palacios, F., Copeland, S. R., Lukaczyk, T. W., and Alonso, J. J., "SU2: An open-source suite for multiphysics simulation and Design," *AIAA Journal,* vol. 54, 2016, pp. 828–846.

[4]   Yildirim, A., Gray, J. S., Mader, C. A., and Martins, J. R., "Aeropropulsive design optimization of a boundary layer ingestion system," AIAA 2019-3455, 2019.

[5]   Turner, R., Eriksson, D., McCourt, M., Kiili, J., Laaksonen, E., Xu, Z., and Guyon, I., "Bayesian optimization is superior to random search for machine learning hyperparameter tuning: Analysis of the black-box optimization challenge 2020," *NeurIPS 2020 Competition and Demonstration Track*, 2021, pp. 3-26.

[6]   Jones, D. R., Schonlau, M., and Welch, W. J., "Efficient global optimization of expensive black-box functions," *Journal of Global Optimization,* Vol.13, No. 4, 1998, pp. 455-492.

[7]   Kosugi, Y., Oyama, A., Fujii, K., and Kanazaki, M., "Multidisciplinary and multi-objective design exploration methodology for conceptual design of a hybrid rocket," AIAA2011-1634, 2011.

[8]   Takenaka, K., Hatanaka, K., Yamazaki, W., and Nakahashi, K., "Multidisciplinary design exploration for a winglet," *Journal of Aircraft*, No.45, Vol.5, 2008, pp. 1601-1611.

[9]   Chiba, K., and Obayashi, S., "Knowledge discovery for flyback-booster aerodynamic wing using data mining," *Journal of Spacecraft and Rockets*, Vol.45, 2008, pp. 975-987.

[10] Obayashi, S., and Sasaki, D., "Visualization and data mining of Pareto solutions using self-organizing map," *International Conference on Evolutionary Multi-Criterion Optimization*, 2003, pp. 796-809.

[11] Chiba, K., Oyama, A., Obayashi, S., Nakahashi, K., and Morino, H., "Multidisciplinary design optimization and data mining for transonic regional-jet wing," *Journal of Aircraft*, Vol.44, 2007, pp. 1100-1112.

[12] Bandaru, S., Ng, A. H. C., and Deb, K., "Data mining methods for knowledge discovery in multi-objective optimization: Part A - survey," *Expert Systems with Applications*, vol. 70, 2017, pp. 139–159.

[13] Bandaru, S., Ng, A. H. C., and Deb, K., "Data mining methods for knowledge discovery in multi-objective optimization: Part B - new developments and applications," *Expert Systems with Applications*, vol. 70, 2017, pp. 119–138.

[14] Gunning, D., Stefik, M., Choi, J., Miller, T., Stumpf, S., and Yang, G.Z., "XAI—explainable artificial intelligence," *Science Robotics*, vol. 4, 2019.

[15] Molnar, C., *Interpretable machine learning: A guide for making Black Box models explainable*, Munich, 2022.

[16] Lundberg, S. M., and Lee, S. I., "A unified approach to interpreting model predictions," *Advances in neural information processing systems 30*, 2017.

[17] Eto, K., Takanashi, S., and Nishimura, S., "Deep Gaussian Process and Deep Sigma Point Process Applied to Aerodynamic Optimization Problem," AIAA2022-2098, 2022.

[18] Gardner, J. R., Pleiss, G., Bindel, D., Weinberger, K. Q., and Wilson, A. G.,"Gpytorch: Blackbox matrix-matrix gaussian process inference with gpu acceleration," *arXiv preprint arXiv:1809.11165*, 2018.

[19] Balandat, M., Karrer, B., Jiang, D. R., Daulton, S., Letham, B., Wilson, A. G., and Bakshy, E., "BoTorch: A Framework for Efficient Monte-Carlo Bayesian Optimization," *Advances in Neural Information Processing Systems 33*, 2020.

[20] Salimbeni, H., and Deisenroth, M., "Doubly stochastic variational inference for deep Gaussian processes," *Advances in neural information processing systems 30*, 2017.

[21] Jankowiak, M., Geoff P., and Jacob G., "Deep sigma point processes," *Conference on Uncertainty in Artificial Intelligence*, 2020, pp. 789-798.

[22] Wilson, J. T., Moriconi, R., Hutter, F., and Deisenroth, M. P., "The reparameterization trick for acquisition functions," *Neural Information Processing Systems Workshop on Bayesian Optimization*, 2017.

[23] Daulton, S., Balandat, M., and Bakshy, E., "Differentiable expected hypervolume improvement for parallel multi-objective Bayesian optimization," *Advances in Neural Information Processing Systems 33*, 2020.

[24] Daulton, S., Balandat, M., and Bakshy, E., "Parallel Bayesian Optimization of Multiple Noisy Objectives with Expected Hypervolume Improvement," *Advances in Neural Information Processing Systems 34*, 2021.

[25] Wilson, J., Hutter, F., and Deisenroth, M., "Maximizing acquisition functions for Bayesian optimization," *Advances in neural information processing systems 31*, 2018.

[26] Shapley, L. S., "A value for n-person games," *Contributions to the Theory of Games (AM-28)*, vol. 2, 1953, pp. 307–318.

[27] Friedman, J. H., "Greedy function approximation: A gradient boosting machine.," *The Annals of Statistics*, vol. 29, 2001.

[28] Nadarajah, S., "AIAA Aerodynamic Design Optimization Group," *McGill Computational Aerodynamics Group* [online database], URL: https://sites.google.com/view/mcgill-computational-aerogroup/adodg [retrieved 11 November 2022].

[29] Roe, P. L., "Approximate Riemann solvers, parameter vectors, and difference schemes," *Journal of Computational Physics*, vol. 43, 1981, pp. 357–372.

[30] Spalart, P., and Allmaras, S., "A One-Equation Turbulence Model for Aerodynamic Flows," AIAA Paper 1992-0439, 1992.

[31] Kulfan, B. M., "Universal parametric geometry representation method," *Journal of Aircraft*, vol. 45, 2008, pp. 142–158.

[32] Sobieczky, H., "Parametric airfoils and Wings," *Notes on Numerical Fluid Mechanics*, 1999, pp. 71–87.

[33] Zhu, F., and Qin, N., "Intuitive class/shape function parameterization for airfoils," *AIAA Journal*, vol. 52, 2014, pp. 17–25.

[34] Morris, M. D., "Factorial sampling plans for preliminary computational experiments," *Technometrics*, vol. 33, 1991, pp. 161–174.

[35] Takenaka, K., Hatanaka,K., Yamazaki, W. and Nakahashi, K., "Multi-Disciplinary Design Exploration for Winglet," *Journal of Aircraft*, vol.45, No.5, pp. 1601-1611, 2008.

[36] Lundberg, S. M., Erion, G., Chen, H., DeGrave, A., Prutkin, J. M., Nair, B., Katz, R., Himmelfarb, J., Bansal, N., and Lee, S.-I., "From local explanations to global understanding with explainable AI for trees," *Nature Machine Intelligence*, vol. 2, 2020, pp. 56–67.

[37] Sobol′, I. M., "Global sensitivity indices for nonlinear mathematical models and their Monte Carlo estimates," *Mathematics and Computers in Simulation*, vol. 55, 2001, pp. 271–280.

[38] Saltelli, A., Ratto, M., Andres, T., Campolongo, F., Cariboni, J., Gatelli, D., Saisana, M., and Tarantola, S., *Global sensitivity analysis: The Primer*, Wiley, Chichester, 2008.

[39] Iwanaga, T., Usher, W., and Herman, J., "Toward salib 2.0: Advancing the accessibility and interpretability of global sensitivity analyses," *Socio-Environmental Systems Modelling*, vol. 4, 2022, p. 18155.

[40] Herman, J., and Usher, W., "Salib: An open-source python library for Sensitivity Analysis," *The Journal of Open Source Software*, vol. 2, 2017, p. 97.